ROYAL SOCIETY
OF CHEMISTRY

PAPER

Check for updates

Constructing P-doped self-assembled V$_2$C MXene/NiCo-layered double hydroxide hybrids toward advanced lithium storage†

Xi Guo,[a] Li Li, [iD] *[a] Shuo Wang,[a] Jian Shen, [iD] [a] Yanan Xu*[b] and Bingqiang Cao [iD] [a]

To strengthen the stability of the anode structure of lithium-ion batteries (LIBs) and enhance the kinetics of their electrochemical reactions, we developed a new strategy to dope phosphorus into a hybrid of NiCo-layered double hydroxide (NiCo-LDH) nanosheets and three-dimensional (3D) multilayered V$_2$C MXene as the anode of high-performance LIBs. Owing to the 3D conductive network and large surface area of 3D V$_2$C multi-layer architectures, we set up a 3D conductive channel for rapid charge transfer and electrolyte storage, making the electrode and electrolyte fully in close contact. MXene, with its unique structure that can effectively resist volume expansion, can avoid the accumulation and breakage of NiCo-LDH nanosheets during the Li$^+$ intercalation/deintercalation process. The synergistic effect between NiCo-LDH and MXene V$_2$C resulted in high structural stability and electrochemical activity of the material and phosphorus atomic doping, which provides richer redox reaction-activated sites with high electrical conductivity and low charge transfer impedance, leading to outstanding electrochemistry performance. The P-doped self-assembled V$_2$C MXene/NiCo-LDH (P-V2C/NiCo-LDH) maintains a specific capacity of 1077 mA h g^{-1} after 700 cycles at a current density of 500 mA g^{-1}. The present strategy of the phosphorus doping route and coupling dual-metallic hydroxide with 3D V$_2$C can be used as novel electrodes for other types of high-performance energy storage devices.

1. Introduction

Electrochemical technologies that constantly seek to be clean, reliable and affordable are playing an increasingly important role in human society, such as electrochemiluminescence technologies,[1] zinc-ion batteries,[2] sodium-ion batteries,[3] and LIBs. In recent years, owing to the extensive application of LIBs in electronic devices, people have been committed to developing LIBs with high energy density, long lifetime, and environmental protection.[4,5] Among the electrochemical transformations, the anodically enabled ones have been far more extensively exploited than those driven by cathodic reduction.[6] However, the commercial graphite-based anodes have only a moderate lithium storage capacity of $\approx$372 mA h g^{-1}, which severely limits their wide application in high-power lithium-ion batteries.[7,8] Therefore, researchers urgently need to develop advanced anode materials with satisfactory cyclic stability and greater reversibility to meet the actual needs of advanced energy storage devices.[9-11]

Two-dimensional (2D) materials, such as graphene, have excellent mobility and flexibility.[12] The layered double hydroxide (LDH), as a material with a two-dimensional structure, has numerous advantages, such as high lithium storage capacity, unique 2D structure, high conductivity and large specific surface areas, which have attracted widespread concern in the realm of energy storage.[13] The general formula of LDH is represented by $[M_{1-x}^{a+}M_x'^{b+}(OH)_2]^{y+}[A_{y/c}^{c-}]^{y+}\cdot zH_2O$, $y = a(1-x) + bx - 2$, where A^{c-} denotes the anion in this layer, and M and M′ denote metal cations.[14] When changing its metal cationic attribute, the anion exchange and structure remain unchanged[15] and could make LDH to be widely applied in the fields of catalysis,[16] biology,[17] sensing,[18] energy conversion and storage.[19] As the demand for energy continues to increase, widespread research has been conducted on energy storage and conversion equipment for alternative energy sources.[20-22] When an anode material is applied to a lithium ion battery, although the LDH has a high specific capacity,[23] the extremely low electronic conductivity, slow ion diffusion capabilities and huge volume changes seriously limit its practical applications.[24] To overcome these shortcomings, it is a feasible solution to convert metal hydroxide into metal oxides by annealing.[25] However, composite materials with matrix materials can also protect the fragile structure without changing the composition and structure of LDH.[23,24] To the best of our

[a] *School of Materials Science and Engineering, University of Jinan, Jinan 250022, Shandong, China. E-mail: mse_lil@ujn.edu.cn*

[b] *Faculty of Education, Tianjin Normal University, Tianjin 300387, China. E-mail: xuyanan2016@126.com*

knowledge, NiCo-LDH is the most representative dihydrogen oxide, and the electrochemical properties have not been fully enhanced.[26,27] In this case, a high hope is to formulate an effective strategy based on surface interaction, which uniformly arranges the ultra-thin NiCo-LDH on a 3D conductive network and an open architecture matrix material. Consequently, the huge changes in the insertion process enhanced electrochemical activity. In particular, owing to the synergy between Co and Ni elements, the multi-oxidation state provides many electrical activity sites, so NiCo-LDH shows good electrochemical performance.[28]

MXenes, fully known as 2D transition metal carbide and nitride, have attracted more and more attention in the field of energy storage devices because of their excellent pseudocapacitive properties,[29–31] high metallic conductivity,[32,33] and modifiable functional groups.[34] The general composition of MXenes is $M_{n+1}X_nT_x$ (where M denotes a transition metal, such as Ti, Zr, V, Nb, Cr, Mo and soon; X denotes C or N; $n = 1$ to 3; and T_x denotes terminal surface functional groups, including –O, –OH and –F), which can be obtained by selectively removing A-atom layers out from the MAX phase.[35–37] The combination of LDH with MXenes is an up-and-coming approach that can strengthen electrochemical dynamics for high-performance electrochemical energy storage equipment. V_2C MXene shows negative electricity owing to the existence of the surface-oriented group, which can easily achieve cationic insertion.[38,39] Because there is a large laminar spacing between MXenes thin slices, inserting the intervals between the MXenes thin tablets can effectively prevent the re-stack of MXenes thin slices, thereby improving its electrochemical performance.[40,41] In addition, the MXene material is a conductor with hydrophilic properties and has high elastic properties as well.[42] Therefore, it exhibits excellent capacity regarding adsorption and can reversibly embed numerous metal ions, such as Li^+, in the edge and interlayer space of MXenes.[38] In addition, heteroatom doping can enhance the conductivity of materials and provide additional activity sites.[43] Recently, boron,[44] nitrogen,[45] phosphorus,[46] and halogen[47] doping of carbon electrodes have demonstrated superior rate performance and outstanding cycling stability in LIBs. Zhang *et al.* introduced red phosphorus nanodot/$Ti_3C_2T_x$ MXenes for superior lithium ion storage, and the capacity of lithium ion battery can be improved to 818.2 mA h g^{-1} after 200 cycles by enhancing P content.[48] Wen *et al.* introduced phosphorus-doped $Ti_3C_2T_x$ MXene nanosheets electrode with a high specific capacitance of 320 F g^{-1} at a current density of 0.5 A g^{-1}.[49] P doping distorts the structure of MXene, leads to more defects, exposes more reaction sites and improves the conductivity, thus improving the electrochemical performance.[50,51]

Based on the aforementioned considerations, a P-doped self-assembled V_2C MXene/NiCo-LDH hybrid was synthesized by applying simple hydrothermal and subsequent calcination methods. The NiCo-LDH on the V_2C effectively inhibits the collapse or re-stack of the V_2C chin layer, and the introduction of P improves the conductivity of composite materials and provides additional activity sites, which significantly enhances the electrochemical performances of LIBs. The morphology, structure and electrochemical properties of the as-prepared

hybrids were systemically characterized and discussed. Obviously, this new design scheme of the NiCo-LDH combination and heteroatom P doping provides a good application basis for preparing high-performance cathode materials.

2. Experimental

2.1. Preparation of 3D V_2C

V_2AlC powders (>99 wt% purity) were bought from Laizhou Kaisen Ceramic Material Co., Ltd. 2 g LiF powders (Shanghai Macklin Biochemical Co., Ltd, 99%) dissolved in 6 M HCl solutions (40 mL) and were left under continuous stirring for 30 min in an ice water bath ($<5\ °C$), followed by the slow addition of V_2AlC powders (2 g) and stirring for 2 h. The solution was then transferred to the stainless steel reactor to maintain heat preservation for 72 h under 90 °C. After the reaction finished, the solution was centrifuged at 3500 rpm and rinsed several times with deionized water until the pH of the supernatant increased to 6. The resulting materials were dried by vacuum drying.

2.2. Preparation of V_2C/NiCo-LDH precursors

$Ni(NO_3)_2 \cdot 6H_2O$, $Co(NO_3)_2 \cdot 6H_2O$, and urea were dissolved in a mixture of deionized water and ethanediol. After the above substances were thoroughly mixed, V_2C (100 mg) was added and stirred continuously for 2 h. Then, the solution was refluxed at 90 °C for 3 h. The precipitate was centrifuged and washed three times with deionized water and anhydrous ethanol and then collected and dried in a vacuum at 60 °C.

2.3. Preparation of P-V_2C/NiCo-LDH hybrids

Using flowing N_2 as a protective atmosphere, phosphorus doping of the precursor was carried out in a tubular furnace. Two porcelain boats were used: one for the precursor and the other for NaH_2PO_2. The porcelain boat with NaH_2PO_2 was located upwind of the quartz tube, and the porcelain boat with precursor was located downwind of the quartz tube. Then, the precursor was calcined at 300 °C in an N_2 atmosphere for 2 hours, with a heating rate of 2 °C min^{-1}. The P-V_2C/NiCo-LDH powders were collected after cooling naturally under flowing N_2.

2.4. Structural characterization

The crystal structures of the products were determined by XRD (BRUKER D8-ADVANCE). The microstructure and morphology were characterized by FESEM (FEI QUANTA FEG250), TEM and HRTEM (FEI Tecnai G2 F20 TEM). The specific states of the elements were characterized by XPS (Thermo ESCALAB 250XI).

2.5. Electrochemical characterization

The electrochemical performance of the electrode was evaluated using a stainless steel button cell (CR 2025). The slurry comprises active materials (V_2C, V_2C/NiCo-LDH, or P-V_2C/NiCo-LDH hybrids, 70 wt%), acetylene black (Super-P, 20 wt%), and polyvinylidene fluoride (PVDF, 10%) with *N*-methylpyrrolidone (NMP) as a solvent. The electrolyte was 1 m $LiPF_6$ in a mixture

of ethylene carbonate and diethyl carbonate (1 : 1 in volume). Cegard 2400 polypropylene membrane and lithium foil were applied as the separator and counter electrode. The representative loading density of the active material on each electrode disk was 0.6–0.8 mg cm^{-2}, the diameter of the copper sheet was about 14 mm, and the mass loading of the active material was about 0.9–1.2 mg. The CR2025-type cells were assembled in a glove box filled with argon with humidity and an oxygen concentration of less than 0.1 ppm. The battery testing system (CT 4008), CHI660E electrochemical workstation (Chenhua Instruments) and Zahner/Zennium electrochemical workstation were used to conduct the galvanostatic charge–discharge experiments, the CV test in the voltage range of 0.01–3.0 V at room temperature, and the EIS analysis from 100 kHz to 100 mHz, respectively.

3. Results and discussion

3.1. Synthesis and characterization

Scheme 1 shows the synthesis path of the P-V$_2$C/NICO-LDH 3D multi-layer structure. The synthesis strategy is described in the following steps. In the first step, LiF/HCl mixed solution was used as an etchant, and multilayer V$_2$C was obtained by *in situ* etching. In this process, Li$^+$ could be spontaneously inserted between V$_2$C layers. V$_2$C/NICO-LDH precursors are used to synthesize P-V$_2$C/NICO-LDH 3D multilayer composites. In this reasonable design process, urea is introduced and dissolved into a solution containing V$_2$C, Ni^{2+} and CO^{2+}. NiCo-LDH was deposited on the surface of the V$_2$C nano-layer by employing the reflux method. The source of phosphorus in the P-V$_2$C/NICO-LDH composite is NaH$_2$PO$_2$. P-V$_2$C/NICO-LDH is obtained by calcining NaH$_2$PO$_2$ with V$_2$C/NiCo-LDH at 300 °C using an *in situ* phosphorus doping process, and the V$_2$C nano-layer still maintains the three-dimensional composite multilayer structure without collapse after calcination.

The phase compositions of the obtained samples were further determined by measuring the X-Ray diffraction (XRD) patterns (Fig. 1(a)). As can be observed from the XRD pattern, the sharp peaks at 13.5° and 41.3° are very consistent with the (002) and (103) crystal planes of V$_2$AlC, respectively. The intensity of the characteristic peaks of the MXene precursor weakens after the etching process; the multilayered V$_2$C nanosheets show a (002) peak around 7.23°, and the (103) peak of V$_2$AlC at 2θ = 41.3° is significantly weakened with the laminar spacing of 12.13 Å, indicating that the Al layer has been selectively etched and the V$_2$AlC phase is transformed into layered V$_2$C MXene.[52,53]
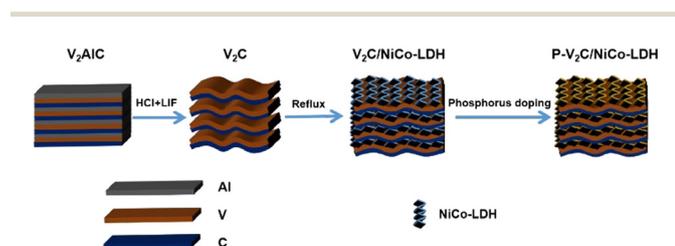
Scheme 1 Schematic showing the preparation processes of P-V$_2$C/NiCo-LDH hybrids.

After the phosphorus-doping process, the (002) peak moves to a large angle, which is mainly due to the removal of interlayer water molecules. Moreover, several sharp diffractions appear at 12.33°, 33.78°, and 60.49°, which can be well assigned to NiCo-LDH.[54,55] The (002) peak of MXene at 7.23° is weakened because the surface LDH nanostructures and the high signal of LDH inhibit the restacking of MXene sheets. It can be observed that the XRD pattern of P-V$_2$C/NiCo-LDH has the same diffraction characteristics as V$_2$C/NiCo-LDH, demonstrating that P-V$_2$C/NiCo-LDH and V$_2$C/NiCo-LDH possess the same crystal structure. It can be reasonably inferred that the crystal structure of V$_2$C/NiCo LDH remains unchanged when the P element is doped into the lattice of V$_2$C/NiCo LDH. The diffraction peaks of NiCo-LDH and V$_2$C after phosphorus doping still exist, which further proves the successful preparation of P-V$_2$C/NiCo-LDH composite materials.

X-ray photoelectron spectroscopy (XPS) was used to study the surface compositions and chemical bond compositions of the obtained materials (Fig. 1(b)). The XPS spectrum of V$_2$C was observed in the presence of C, O, V, and F elements, where the F element was introduced owing to LiF during the etching process. The XPS survey scan confirms that Co, Ni, O, V, P and C elements coexist in P-V$_2$C/NiCo LDH. For the high-resolution XPS spectrum of O 1s/V 2p (Fig. 1(c)), it can be deconvoluted into three peaks at the binding energies of 530.3, 531.8 and 533.6 eV, which correspond to V–O, V–O–H and H–O–H, respectively.[56,57] Compared with the O 1s/V 2p diagram of V$_2$C (Fig. S1a, ESI†), the V^{2+} feature peak disappeared, and the peak strength of V–O was increased because of the oxidation of the part of V during the annealing process.[56,57] In addition, the shift to higher energy indicates that V undergoes a charge transfer process after phosphorus doping. Analysis of the high-resolution XPS spectrum of C 1s of P-V$_2$C/NiCo-LDH (Fig. 1(d)) shows four convolution peaks with binding energies of 284.6, 285.1, 286.2 and 288.9 eV, corresponding to C–C, C–H, C–O and O=C–O. Compared with the C 1s diagram of V$_2$C (Fig. S1b, ESI†), the peak of C–V, caused by introducing NiCo-LDH, at 282.1 eV disappears.[39,58] As shown in Fig. 1(e), Ni 2p spectrum shows four significant peaks. The peaks at 856.45 eV and 874.05 eV belong to Ni 2p3/2 and Ni 2p1/2, respectively, and the corresponding satellite peaks of Ni 2p3/2 and Ni 2p1/2 are located at 962.5 and 880.65 eV, respectively.[59] The high-resolution Co 2p spectrum shows four prominent peaks, as shown in Fig. 1(f), and the peaks at 797.7 and 781.56 eV are assigned to Co 2p1/2 and Co 2p3/2, respectively, along with two satellite peaks at 786.8 and 803.65 eV.[60] The XPS data demonstrate the successful preparation of P-V$_2$C/NiCo-LDH.

The multilayered V$_2$C exhibits an accordion-like morphology instead of the block of V$_2$AlC from the SEM images in Fig. 2(a) and Fig. S2a (ESI†). The TEM image of V$_2$C shown in Fig. S2b (ESI†) reveals the obvious multilayered structure of V$_2$C nanosheets, and the corresponding layer spacing is about 1.217 nm. For the V$_2$C/NiCo-LDH and P-V$_2$C/NiCo-LDH nanohybrids, the SEM images (Fig. 2(b) and (c)) indicate the growth of loosely flaky texture of NiCo-LDH nanosheets on the few-layer V$_2$C surface. The monodispersed NiCo-LDH 2D nanosheets with
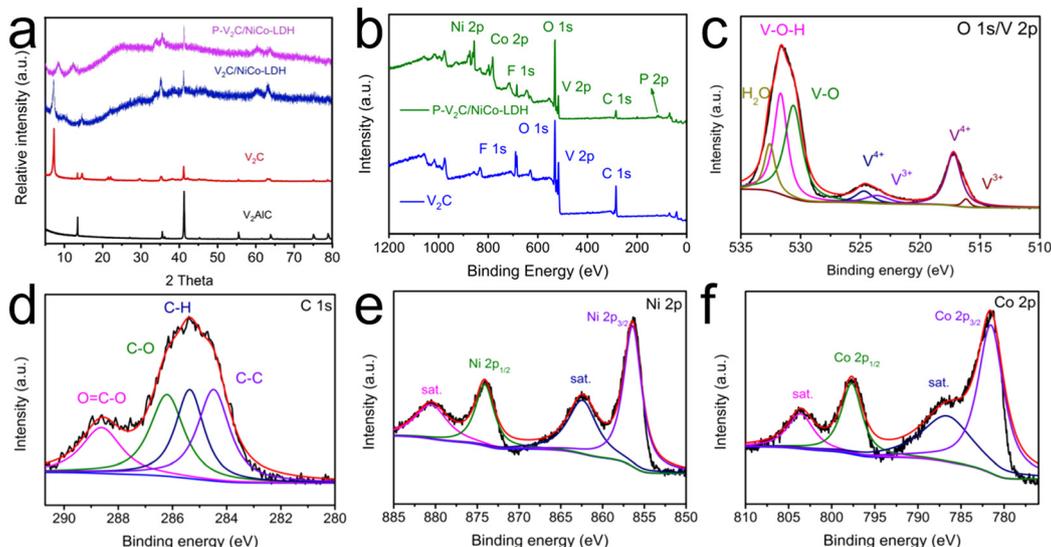
Fig. 1   (a) XRD patterns of V_2AlC, V_2C, $V_2C/NiCo$-LDH, and P-$V_2C/NiCo$-LDH samples. (b) XPS survey spectra of V_2C and P-$V_2C/NiCo$-LDH. (c)−(f) High-resolution XPS spectra of O 1s/V 2p, C 1s, Ni 2p and Co 2p in the P-$V_2C/NiCo$-LDH hybrids.

a uniform size of about 100 nm are homogeneously embedded in the V_2C nanosheets. In addition, this flaky morphology is ideal for promoting mass diffusion and charge transfer in an electrochemical reaction.[61] The TEM images depicted in Fig. 2(d) and (e) show that the NiCo-LDH 2D nanosheets grow uniformly on the V_2C surface, which agrees with the SEM results. In addition, the selected area electron diffraction (SAED) pattern

of P-$V_2C/NiCo$-LDH (Fig. 2(e)) significantly differs from the SAED of the V_2C (Fig. S2c, ESI†)[62] owing to the formation of the surface NiCo-LDH with several diffraction rings,[63] verifying that the NiCo-LDH nanosheets have a polycrystalline structure. The lattice spacings of 0.28 nm, 0.237 nm, and 0.262 nm shown by high-resolution TEM (HRTEM) observation (Fig. 2(f) and Fig. S2c, ESI†) correspond to the (002) plane of V_2C and the
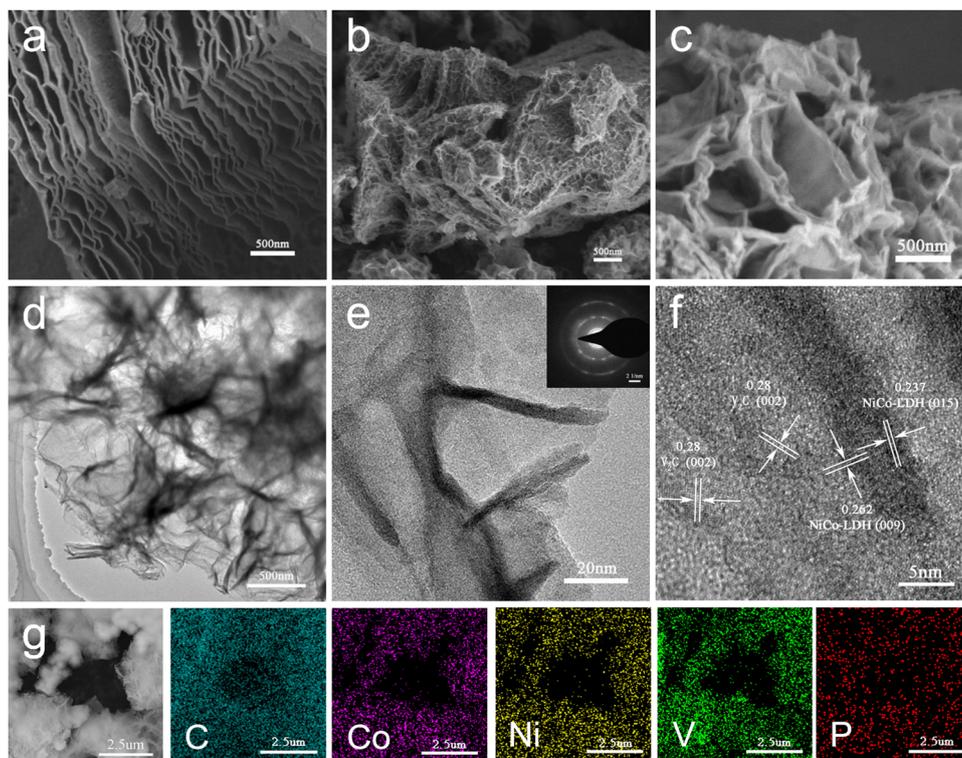

Fig. 2   SEM images of the (a) V_2C nanosheets, (b) $V_2C/NiCo$-LDH, and (c) P-$V_2C/NiCo$-LDH hybrids. (d) and (e) TEM images of P-$V_2C/NiCo$-LDH hybrid; the inset corresponds to the SAED pattern of P-$V_2C/NiCo$-LDH. (f) HRTEM image of P-$V_2C/NiCo$-LDH. (g) EDS results of P-$V_2C/NiCo$-LDH hybrids.

(015) and (009) planes of NiCo-LDH,[59,64,65] respectively, confirming the formation of NiCo-LDH on the V_2C surface. The EDS results in Fig. 2(g) show a good overlap in the characteristic regions of C, Co, Ni, and V, in which the NiCo-LDH nanoplates mapped with Ni and Co elements cover multiple layers of V_2C, while the P is uniformly distributed, indicating that the NiCo-LDH nanoplate array is uniformly array is uniformly arranged on multi-layer V_2C and P is uniformly doped. For comparison, SEM and EDS images of V_2C/NiCo-LDH nano-hybrid are also analyzed, as shown in Fig. S3 (ESI†), which have similar lamellar morphology and uniformly distributed elements of C, Co, Ni and V.

3.2. Electrochemical properties

As discussed above, the as-synthesized P-V_2C/NiCo-LDH, which is expected to be a potential substitute anode material for LIBs, has a unique structural advantage. The representative cyclic voltammetry (CV) curves of P-V_2C/NiCo-LDH for the first to third cycles at 0.2 mV s^{-1} in the potential range from 0.01 to 3.0 V (*vs.* Li/Li$^+$) were observed, as shown in Fig. 3(a), to analyze the Li-storage mechanism. In the first cathodic sweep, two irreversible reduction peaks are evidently located at $\approx$1.2 and $\approx$0.7 V, which can be assigned to the reduction reactions of Co^{2+} to Co and Ni^{2+}

to Ni, respectively. Regarding the anode scan, two apparent oxidation peaks are observed near 1.4 V and 2.3 V, corresponding to two oxidation steps of Co to Co(OH)$_2$ and Ni to Ni(OH)$_2$ during the multi-level oxidation processes, accompanied by a decomposition of Li$_2$O. As previously mentioned, the subsequent cycles in the cathodic process completely differ from the initial cycle. After the first cycle, the cathode peak of 1.2 V disappears, and one distinguished peak at $\approx$1.7 V is detected in the following cathodic processes, corresponding to the formation of the solid electrolyte interphase (SEI) layer.[66] In the subsequent cycles in the anodic process, four weak anodic peaks were formed at 1.2, 1.4, 1.8 and 2.3 V. The two peaks at 1.4 and 2.3 V are attributed to the oxidation processes of Co and Ni, while the two peaks at 1.2 and 1.8 V are attributed to the separation of Li$^+$ from the V_2C layer. Furthermore, the CV curves are completely consistent in the subsequent cycle, indicating that P-V_2C/NiCo LDH electrode had extremely high reversibility and excellent cycling stability in the Li$^+$ insertion/extraction process. Based on CV analysis, the discharge/charge processes of the P-V_2C/NiCo-LDH electrode can be rationally inferred and expressed using the following equations:[23,26,67,68]
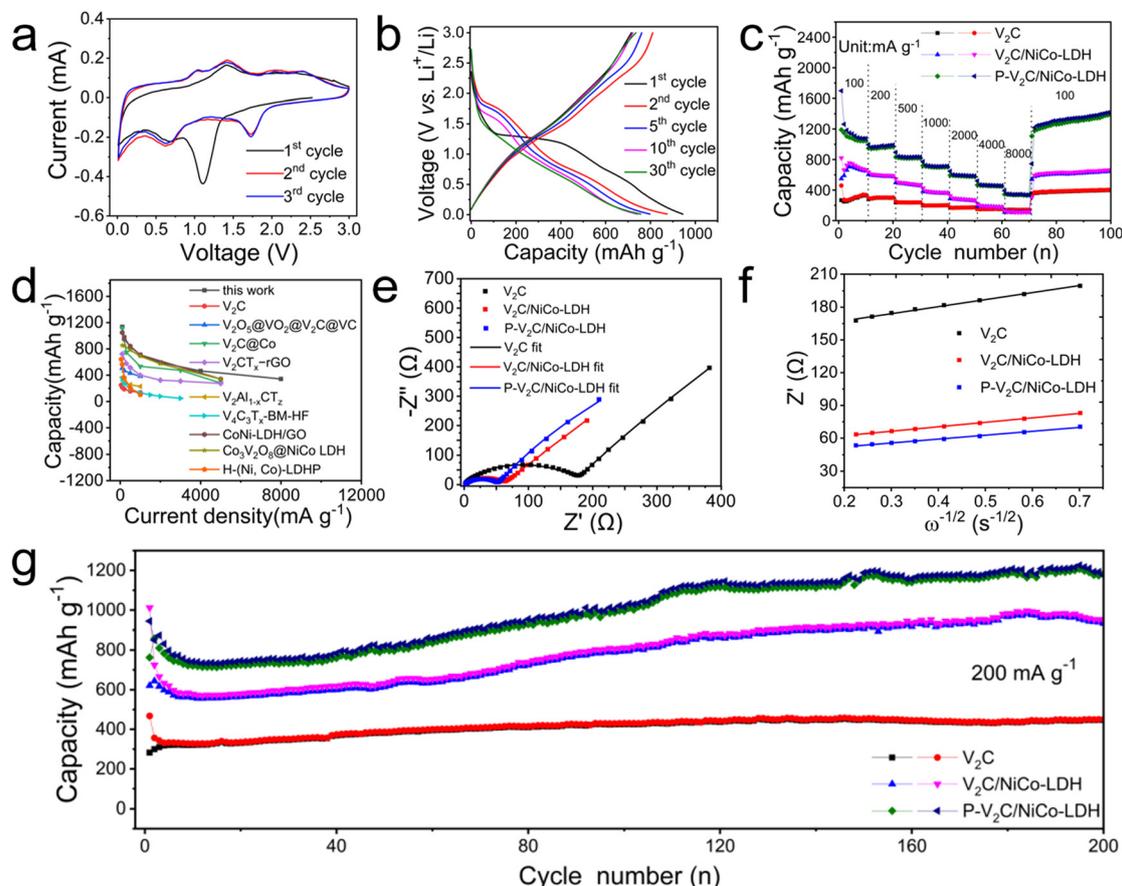
$$V_2C + xLi^+ + xe^- \leftrightarrow Li_xV_2C, \tag{1}$$

Fig. 3 (a) CV curves and (b) selected galvanostatic charge–discharge profiles of the P-V_2C/NiCo-LDH electrode. (c) Rate behaviors of V_2C, V_2C/NiCo-LDH, and P-V_2C/NiCo-LDH electrodes at various rates. (d) Comparisons in rate capabilities between P-V_2C/NiCo-LDH and other V_2C- and NiCo-LDH-based electrodes. (e) EIS and corresponding fitted plots, and (f) relationship between Z' and $\omega^{-1/2}$ in the low-frequency region of the V_2C, V_2C/NiCo-LDH, and P-V_2C/NiCo-LDH electrodes. (g) Cycling behaviors of V_2C, V_2C/NiCo-LDH, and P-V_2C/NiCo-LDH electrodes as indicated.

$$Co(OH)_2 + 2Li^+ + 2e^- \leftrightarrow Co + 2LiOH, \quad (2)$$

$$Ni(OH)_2 + 2Li^+ + 2e^- \leftrightarrow Ni + 2LiOH, \quad (3)$$

$$LiOH + 2Li^+ + 2e^- \leftrightarrow Li_2O + LiH. \quad (4)$$
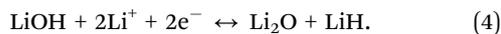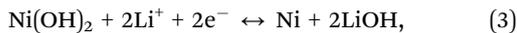
Fig. 3(b) shows the galvanostatic charge–discharge curves of the P-V$_2$C/NiCo-LDH anode at the 1st, 2nd, 5th, 10th and 30th turns. The noteworthy potential plateaus in the figure agree well with the above CV analysis. The initial discharge/charge capacities of the P-V$_2$C/NiCo-LDH are estimated as ≈ 944/≈ 714 mA h g^{-1} at 200 mA g^{-1}, corresponding to high initial Coulombic efficiencies (CE) of $\approx 75.6\%$. The irreversible capacity loss of the battery is less than 25%, which can be reasonably considered the extra lithium consumption in the process of forming the SEI layer. It is noteworthy that the initial discharge/charge capacity of V$_2$C/NiFe-LDH is ≈ 1012/≈ 620 mA h g^{-1}, and it can be concluded that the initial CE at 200 mA g^{-1} is 61.3% (Fig. S4a, ESI†). Additionally, the specific discharge capacity of V$_2$C is only ≈ 467 mA h g^{-1}, and the corresponding initial CE value of $\approx 60.4\%$ (Fig. S4b, ESI†). In the 30th cycle at 200 mA g^{-1}, the P-V$_2$C/NiCo-LDH shows a large discharge/charge capacities of ≈ 756/≈ 735 mA h g^{-1}, which are higher than that of the V$_2$C/NiCo-LDH (≈ 603/≈ 585 mA h g^{-1}) (Fig. S4a, ESI†) and V$_2$C (≈ 350/≈ 346 mA h g^{-1}) (Fig. S4b, ESI†). The higher initial CE and reversible capacities observed in P-V$_2$C/NiCo-LDH, compared to the V$_2$C and V$_2$C/NiCo-LDH, highlight the positive contributions of the stable 3D-layered architecture to the enhanced electrolyte storage and Li$^+$ transfer behaviors. In addition to the improvement in conductivity caused by the introduction of NiCo-LDH, many doped phosphorus atoms further increase the number of electroactive sites and improve the electronic conductivity, contributing to the effective electrochemical reaction of P-V$_2$C/NiCo-LDH.

To further identify the virtues of the P-V$_2$C/NiCo-LDH for LIBs, the rate capabilities of V$_2$C, V$_2$C/NiCo-LDH, and P-V$_2$C/NiCo-LDH are comparatively carried out, as shown in Fig. 3(c). Noticeably, P-V$_2$C/NiCo-LDH exhibits reversible discharge specific capacities of 1139, 977, 832, 712, 594 and 456 mA h g^{-1} when the applied current densities are 100, 200, 500, 1000, 2000 and 4000 mA g^{-1}, respectively. These values far exceed the reversible capacity of the V$_2$C/NiCo-LDH electrode of ≈ 704 and ≈ 109 mA h g^{-1} at the current densities of 100 and 4000 mA g^{-1}, respectively. What is particularly noteworthy is that even at a super high current density of 8000 mA g^{-1}, a competitive capacity of ≈ 343 mA h g^{-1} is still maintained by the P-V$_2$C/NiCo-LDH. At 8000 mA g^{-1}, the V$_2$C and V$_2$C/NiCo-LDH electrodes retain only the discharge capacities of ≈ 141 and ≈ 109 mA h g^{-1}, respectively. In addition, as the current density further immediately drops to 100 mA g^{-1}, the capacity of P-V$_2$C/NiCo-LDH can be restored to ≈ 1378 mA h g^{-1}, along with the recovered capacities of ≈ 384 and ≈ 629 mA h g^{-1} for the V$_2$C and V$_2$C/NiCo-LDH, respectively. P-V$_2$C/NiCo-LDH electrode demonstrates more outstanding rate capability in the rate range of 100–8000 mA g^{-1}, which considerably proves that the introduced NiCo-LDH and phosphorus doping play a decisive role in the excellent electrochemical performance of P-V$_2$C/NiCo-LDH anode. What is more

important, as comparatively exhibited in Fig. 3(d), is that the rate performance of the P-V$_2$C/NiCo-LDH electrode obtained here is superior to other V$_2$C- and NiCo-LDH-based anodes previously reported,[39,55,58–60,69–72] especially at large current density. When the current density is 1000 mA g^{-1}, the discharge specific capacities of materials, such as CoNi-LDH/GO (710.2 mA h g^{-1}),[55] Co$_3$V$_2$O$_8$@-NiCo-LDH (689 mA h g^{-1}),[60] V$_2$C@Co (535 mA h g^{-1}),[39] and V$_2$O$_5$@VO$_2$@V$_2$C@VC (382 mA h g^{-1})[70] shown in Fig. 3(d) are smaller than the discharge specific capacities of P-V$_2$C/NiCo-LDH(712 mA h g^{-1}). The discharge specific capacity of P-V$_2$C/NiCo-LDH(343 mA h g^{-1}) at the current density of 8000 mA g^{-1} is larger than that of CoNi-LDH/GO(342.3 mA h g^{-1}),[55] Co$_3$V$_2$O$_8$@-NiCo-LDH(342 mA h g^{-1}),[60] V$_2$C@Co(281 mA h g^{-1}),[39] and V$_2$CT$_x$-rGO(275 mA h g^{-1})[71] at the current density of 5000 mA g^{-1}.

Electrochemical impedance spectroscopy (EIS) analysis was carried out to determine the main reason for the excellent rate performance of P-V$_2$C/NiCo-LDH. Typical Nyquist diagrams of V$_2$C, V$_2$C/NiCo-LDH and P-V$_2$C/NiCo-LDH electrodes, as shown in Fig. 3(e), match the equivalent circuit model (Fig. S5, ESI†). As illustrated in Fig. 3(e), charge transfer resistances (R_{f+ct}) and various SEI layer resistances are represented by the semicircles with different diameters.[73] Evidently, the P-V$_2$C/NiCo-LDH exhibits a much smaller R_{f+ct} (≈ 49 ohm) compared to those of the V$_2$C (≈ 171 Ohm) and V$_2$C/NiCo-LDH (≈ 57 ohm), which convincingly validates the fast electron/ion transfer in the P-V$_2$C/NiCo-LDH electrode due to the synergistic effects of the doped phosphorus and NiCo-LDH in V$_2$C. The small R_{f+ct} value corresponds to the fast electron/ion transfer trait in the P-V$_2$C/NiCo-LDH electrode. In addition, the lithium ion diffusion coefficient (D) of the electrode can be calculated from the EIS data, and the calculation formula is as follows:

$$D = (R^2 T^2)/(2A^2 n^4 F^4 C^2 \sigma^2), \quad (5)$$

$$Z' = R_D + R_L + \sigma\omega^{-1/2}, \quad (6)$$

where R, T, A, n, F, C, σ, and ω correspond to the gas constant, absolute temperature, surface area, the number of transferred electrons, Faraday constant, concentration of lithium ions, Warburg factor, and angular frequency ($\omega = 2\pi f$).[74,75] Therefore, the Warburg factor σ as a function of $\omega^{-1/2}$ can be obtained from Z' (Fig. 3(f)). The slopes of Z' *versus* $\omega^{-1/2}$ for the V$_2$C, V$_2$C/NiCo-LDH and P-V$_2$C/NiCo-LDH electrodes are fitted as 65, 54, and 35, respectively. Hence, because other parameters are the same, the D values qualitatively conform to the following order: P-V$_2$C/NiCo-LDH > V$_2$C/NiCo-LDH > V$_2$C. It is evident from the above results that P-V$_2$C/NiCo-LDH has a higher D value than V$_2$C and V$_2$C/NiCo-LDH. It is concluded that the rapid electron/ion diffusion and lower electrical resistance are the main reasons why P-V$_2$C/NiCo-LDH electrode has super rate performance. Fig. 3(g) illustrates the cycle performance of the prepared V$_2$C, V$_2$C/NiCo-LDH and P-V$_2$C/NiCo-LDH electrodes. Obviously, after 200 charge–discharge cycles at 200 mA g^{-1}, the discharge specific capacity of V$_2$C/NiCo-LDH still remains at ≈ 958 mA h g^{-1}, while the discharge capacity of V$_2$C decrease to only ≈ 446 mA h g^{-1}. Additionally, under the current density of 200 mA g^{-1}, the P-V$_2$C/NiCo-LDH electrode further obtains a

high discharge capacity of ≈1217 mA h g^{-1} after 200 cycles. Even after 300 charge–discharge cycles at a current density of 500 mA g^{-1}, it still maintains a high discharge capacity of ≈941 mA h g^{-1} (Fig. 4(a)), which reveals the superior cycle stability of P-V$_2$C/NiCo-LDH. In contrast, V$_2$C and V$_2$C/NiCo-LDH only achieved low discharge specific capacities of ≈313 mA h g^{-1} and ≈844 mA h g^{-1} after 300 cycles at 500 mA g^{-1}, respectively (Fig. S6, ESI†). It can be concluded from the above results that P doping is the main reason for the excellent capacity retention rate of the P-V$_2$C/NiCo-LDH electrode, and the charger transfer kinetics and electrochemical redox kinetics are significantly improved by the P doping strategy.

For the commercial application of LIBs, long-term cycle stability at a high current density is a very important performance characteristic. Therefore, to study the long-term cycling stability of the P-V$_2$C/NiCo-LDH electrode, 700 uninterrupted cycles were carried out at a high current density of 500 mA g^{-1}. As shown in Fig. 4(a), we can observe that there is a capacity fluctuation at the beginning of the cycle curve, in which the rapid decrease in capacity is caused by lithium-induced mechanical degradation and the formation of SEI; the continuous increase in capacity is caused by continuous high-rate lithiation

Fig. 4 (a) High-rate cycling performance and CE data at 500 mA g^{-1} of P-V$_2$C/NiCo-LDH. Cross-section FESEM images of the (b) fresh and (c) cycled P-V$_2$C/NiCo-LDH electrodes. Surface FESEM images of the (d) fresh and (e) cycled P-V$_2$C/NiCo-LDH electrodes.

reactivating the electrode materials.[76] The discharge capacity of P-V$_2$C/NiCo-LDH is finally maintained at ≈1077 mA h g^{-1}, and the Coulombic efficiency is maintained above 99%. It is noteworthy that the fluctuations of the capacity curve in a small range are attributed to the fluctuation of the ambient temperature during the battery cycle.[77] The exceptional high-rate cyclic performance of P-V$_2$C/NiCo-LDH is reasonably attributed to the remarkable supporting effect of nanoscale NiCo-LDH on the structural stability of the multilayer V$_2$C structure. It can effectively buffer the volume expansion, inhibit the excessive aggregation of NiCo-LDH, and ensure the structural stability of the P-V$_2$C/NiCo-LDH anode. The FESEM of the cross-section anode before and after the cycle (Fig. 4(b) and (c)) shows that the thickness of the anode of P-V$_2$C/NiCo-LDH slightly increases from 7.1 um to 7.4 um after 250 cycles, with only 0.04% volume expansion, which verifies the above conclusion.[78–81] In addition, as shown in Fig. 4(d) and (e), compared with the P-V$_2$C/NiCo-LDH electrode before the cycle, the P-V$_2$C/NiCo-LDH electrode after the cycle has a smooth surface without any cracks that highlights the strong structural stability of the hybrid electrode during the high-rate cycle.

To explore the Li$^+$ storage kinetics of V$_2$C/nico-LDH and P-V$_2$C/nico-LDH electrodes, an in-depth kinetic analysis was conducted based on the CV curves obtained at different scanning rates (0.1–2.0 mV s^{-1}) (Fig. 5(a) and Fig. S7a, ESI†). The relation equation between the peak current (i) and the scanning rate (v)[82–84] is as follows:

$$i = av^b = k_1v + k_2v^{0.5}. \qquad (7)$$

By fitting the slope of the log(i) *vs.* log(v) curve (Fig. 5(b) and Fig. S7b, ESI†), the values of B were calculated. Based on the calculated B values of peaks 1, 2, 3, 4, 5 and 6, which correspond to 0.68, 0.90, 0.89, 0.86, 0.82 and 0.87, it is proved that diffusion and capacitance behavior jointly control the electrochemical response process of V$_2$C/NiCo-LDH electrode. In addition, the b values of P-V$_2$C/NiCo-LDH are 0.72, 0.90, 0.87, 0.78, 0.87 and 0.85, respectively, illustrating that the electrochemical response process of the P-V$_2$C/NiCo-LDH electrode is mainly dominated by capacitance contributions. The capacitance contribution rates of P-V$_2$C/NiCo-LDH and V$_2$C/NiCo-LDH are calculated to be 85% and 83%, respectively, according to the CV curves (Fig. 5(c) and Fig. S7c, ESI†) when the scanning rate increases to 2 mV s^{-1}. As depicted in Fig. 5(d), the capacitance contributions in the P-V$_2$C/NiCo-LDH electrode are estimated as 54%, 68%, 73%, 76%, 80% and 85% at 0.1, 0.3, 0.5, 0.7, 1 and 2 mV s^{-1}, respectively. As shown in Fig. S7d (ESI†), the capacitance contribution ratios of V$_2$C/NiCo-LDH at different scanning rates are also obtained by calculation based on CV data. Obviously, the capacitance contributions of P-V$_2$C/NiCo-LDH are larger than those of V$_2$C/NiCo-LDH in all scanning rate ranges, which can be attributed to the improvement in the rate capability of P-V$_2$C/NiCo-LDH. Obviously, in the total capacity of P-V$_2$C/NiCo-LDH, the normal capacitance contribution occupies a high proportion, which may be due to its rich surface/interface, which is beneficial for the storage of pseudo-
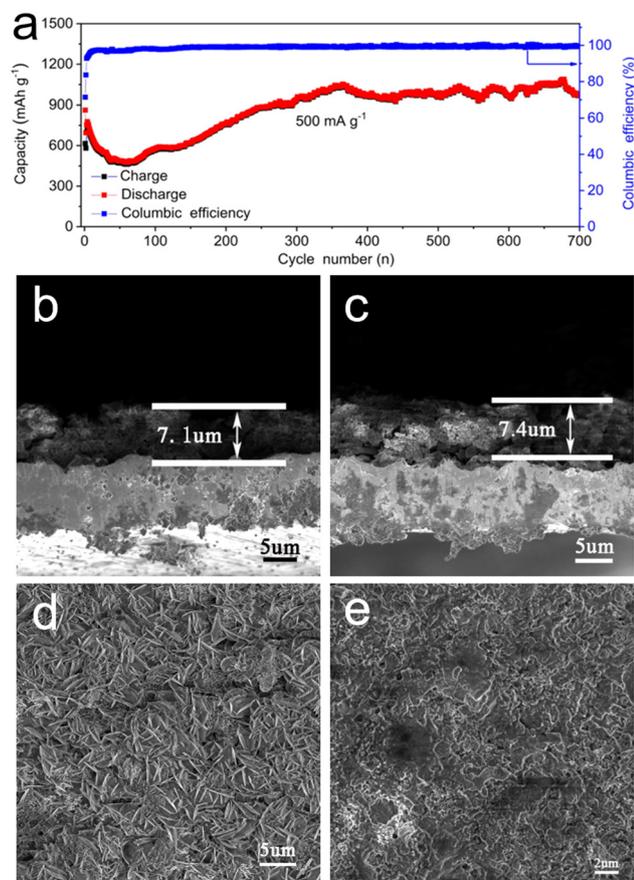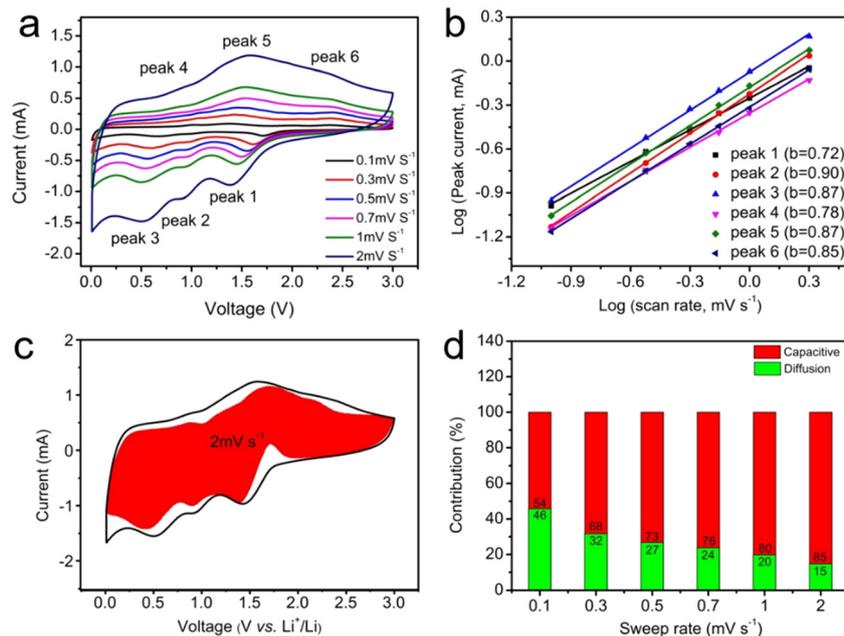
Fig. 5 (a) CV curves of the P-V$_2$C/NiCo-LDH electrode at different scan rates, as indicated. (b) Relationship between peak current and scan rate at different scan rates. (c) CV profile at 2 mV s^{-1} with the capacitive contribution (red region). (d) Normalized contribution ratios of the capacitive (red) and diffusion-dominated (green) capacities at various sweep rates based on quantitative analysis.

capacitance lithium in the hybrid anode. Therefore, even at a high scanning rate, P-V$_2$C/NiCo-LDH has a larger reversible capacity and a longer cycle stability.

The excellent electrochemical performance of the P-V$_2$C/NiCo-LDH electrode can be attributed to the following unique features. (1) The scattered NiCo-LDH is uniformly distributed on the multilayered V$_2$C, allowing the synergy between Ni and Co ions to be fully used. (2) Many open multilayers in a stable 3D layered structure are beneficial to electrolyte storage, provide a fast channel for Li$^+$ transfer, and make the contact between the electrode and electrolyte closer. (3) The introduction of the P atom in P-V$_2$C/NiCo-LDH makes the prepared hybrid have more reaction sites and higher conductivity, thus improving electrochemical performance.

4. Conclusions

In summary, a unique 3D multilayer architecture P-V$_2$C/NiCo-LDH hybrid is synthesized by a solvothermal reaction and phosphorus doping in calcination, which is characterized by the fact that NiCo-LDH was uniformly modified on V$_2$C nanosheets. This unique structure is beneficial for relieving the volume expansion of the anode and for effectively improving the kinetics. Owing to the synergistic effect among the components in the hybrid, the P-V$_2$C/NiCo-LDH electrode has high structural stability and electrochemical activity, resulting in excellent electrochemical performance. This shows that after 700 cycles at a current density of 500 mA g^{-1}, the specific capacity remains at 1077 mA h g^{-1}. The multi-layer stable 3D layered structure has numerous open interlayer areas. The electrode materials and electrolytes can be fully and closely contacted, which is conducive to electrolyte storage

and provides smooth channels for Li$^+$ transfer. The growth of NiCo-LDH and the introduction of doping phosphorus atoms provide richer reaction activity sites, higher conductivity, and enhanced electrochemical properties for multi-layered V$_2$C. The present strategy for the phosphorus doping route and coupling LDH with 3D V$_2$C MXene can be extended to other advanced hybrid anodes for high-performance energy storage devices. In the future, the strategy of coupling LDH with 3D V$_2$C MXene and the route of phosphorus doping can be extended to the application of high-performance energy storage equipment and the synthesis of other advanced mixed anode materials.

Conflicts of interest

There are no conflicts to declare.

Acknowledgements

Notes and references

1 C. D. Meng, S. Knežević, F. X. Du, Y. R. Guan, F. Kanoufi, N. Sojic and G. B. Xu, Recent advances in electrochemiluminescence imaging analysis, *eScience*, 2022, **2**, 591–605.

2 Y. Tan, F. Q. An, Y. C. Liu, S. W. Li, P. G. He, N. Zhang, P. Li and X. H. Qu, Reaction kinetics in rechargeable zinc-ion batteries, *J. Power Sources*, 2021, **492**, 229655.

3 Y. K. Liu, J. Li, Q. Y. Shen, J. Zhang, P. G. He, X. H. Qu and Y. C. Liu, Advanced characterizations and measurements

for sodium-ion batteries with NASICON-type cathode materials, *eScience*, 2022, **2**, 10–31.

4 L. W. Liang, X. Sun, J. Y. Zhang, L. R. Hou, J. F. Sun, Y. Liu, S. G. Wang and C. Z. Yuan, *In situ* synthesis of hierarchical core double-shell Ti-doped $LiMnPO_4@NaTi_2(PO_4)_3@C$/3D graphene cathode with high-rate capability and long cycle life for lithium-ion batteries, *Adv. Energy Mater.*, 2019, **9**, 1802847.

5 D. D. Yin, H. Y. Zhao, N. Li, R. Si, X. L. Sun, X. H. Li and Y. P. Du, Enhancing the rate capability of niobium oxide electrode through rare-earth doping engineering, *Batteries Supercaps*, 2019, **2**, 924–928.

6 B. B. Huang, Z. M. Sun and G. B. Sun, Recent progress in cathodic reduction-enabled organic electrosynthesis: trends, challenges, and opportunities, *eScience*, 2022, **2**, 243–277.

7 Y. F. Shen, J. F. Qian, H. X. Yang, F. P. Zhong and X. X. Ai, Chemically prelithiated hard-carbon anode for high power and high capacity Li-ion batteries, *Small*, 2020, **16**, 1907602.

8 Y. Q. Zhang, L. Tao, C. Xie, D. D. Wang, Y. Q. Zou, R. Chen, Y. Y. Wang, C. K. Jia and S. Y. Wang, Defect engineering on electrode materials for rechargeable batteries, *Adv. Mater.*, 2020, **32**, 1905923.

9 L. Zhou, J. Zhang, Y. Q. Wu, W. X. Wang, H. Ming, Q. J. Sun, L. M. Wang, J. Ming and H. N. Alshareef, Understanding Ostwald ripening and surface charging effects in solvothermally-prepared metal oxide-carbon anodes for high performance rechargeable batteries, *Adv. Energy Mater.*, 2019, **9**, 1902194.

10 L. Ye, Y. T. Zhou, Y. G. Zhao, L. Y. Feng, Z. Wen, L. J. Zhao and Q. Jiang, Engineering oxygen vacancy on iron oxides/hollow carbon cloth electrode toward stable lithium-ion batteries, *Chem. Eng. J.*, 2020, **388**, 124229.

11 X. J. Xu, J. Liu, Z. B. Liu, Z. S. Wang, R. Z. Hu, J. W. Liu, L. Z. Ouyang and M. Zhu, FeP@C nanotube arrays grown on carbon fabric as a low potential and freestanding anode for high-performance Li-Ion batteries, *Small*, 2018, **14**, 1800793.

12 T. Huang, J. F. Ding, Z. R. Liu, R. Zhang, B. L. Zhang, K. Xiong, L. Z. Zhang, C. Wang, S. L. Shen, C. Y. Li, P. Yang and F. Qiu, Insight into the underlying competitive mechanism for the shift of the charge neutrality point in a trilayer-graphene field-effect transistor, *eScience*, 2022, **2**, 319–328.

13 H. T. Xiong, L. L. Liu, L. Fang, F. Wu, S. F. Zhang, H. J. Luo, C. Z. Tong, B. S. Hu and M. Zhou, 3D self-supporting heterostructure NiCo-LDH/ZnO/CC electrode for flexible high-performance supercapacitor, *J. Alloys Compd.*, 2021, **857**, 158275.

14 M. W. Laipan, J. F. Yu, R. L. Zhu, J. X. Zhu, A. T. Smith, H. P. He, D. O'Hare and L. Y. Sun, Functionalized layered double hydroxides for innovative applications, *Mater. Horiz.*, 2020, **7**, 715–745.

15 D. Wang, J. L. Wu, D. X. Bai, R. R. Wang, F. Yao and S. L. Xu, Mesoporous spinel ferrite composite derived from a ternary MgZnFe-layered double hydroxide precursor for lithium storage, *J. Alloys Compd.*, 2017, **726**, 306–314.

16 G. L. Fan, F. Li and D. G. Evans, X. Duan, Catalytic applications of layered double hydroxides: recent advances and perspectives, *Chem. Soc. Rev.*, 2014, **43**, 7040–7066.

17 B. Kutlu, A. Leuteritz, R. Boldt, D. Jehnichen, U. Wagenknecht and G. Heinrich, PANI-LDH prepared by polymerization-adsorption method and processing to conductive compounds, *Appl. Clay Sci.*, 2013, **72**, 91–95.

18 L. L. Wang, J. H. Li, Y. B. Zhao, H. J. He, L. L. Zheng, Z. J. Huang, X. Zhao, J. Q. Xu, B. Wang and Z. Yin, Engineering of a self-supported carbon electrode with 2D ultrathin heterostructures of NiCo LDH/NiCoS *via* a MOF-template for sensitive detection of glucose and H_2O_2, *Mater. Adv.*, 2022, **3**, 6028–6036.

19 J. S. Luo, J. H. Im, M. T. Mayer, M. Schreier, M. K. Nazeeruddin, N.-G. Park, S. D. Tilley, H. J. Fan and M. Grätzel, Water photolysis at 12.3% efficiency *via* perovskite photovoltaics and Earth-abundant catalysts, *Science*, 2014, **345**, 1593–1596.

20 J. J. Liu, T. He, Q. C. Wang, Z. X. Zhou, Y. Q. Zhang, H. Q. Wu, Q. Li, J. Zheng, Z. F. Sun, Y. P. Lei, J. M. Ma and Y. Zhang, Confining ultrasmall bimetallic alloys in porous N-carbon for use as scalable and sustainable electrocatalysts for rechargeable Zn–air batteries, *J. Mater. Chem. A*, 2019, **7**, 12451–12456.

21 G. Z. Fang, Q. C. Wang, J. Zhou, Y. P. Lei, Z. X. Chen, Z. Q. Wang, A. Q. Pan and S. Q. Liang, Metal organic framework-templated synthesis of bimetallic selenides with rich phase boundaries for sodium-ion storage and oxygen evolution reaction, *ACS Nano*, 2019, **13**, 5635–5645.

22 C. S. Lei, W. Zhou, Q. G. Feng, Y. P. Lei, Y. Zhang, Y. Chen and J. Q. Qin, Charge engineering of Mo_2C@defect-rich N-doped carbon nanosheets for efficient electrocatalytic H_2 evolution, *Nano-Micro Lett.*, 2019, **11**, 45.

23 Y.-S. He, D.-W. Bai, X. W. Yang, J. Chen, X.-Z. Liao and Z.-F. Ma, A $Co(OH)_2$−graphene nanosheets composite as a high performance anode material for rechargeable lithium batteries, *Electrochem. Commun.*, 2010, **12**, 570–573.

24 Z. Yuan, H. Y. Wang, J. L. Shen, P. C. Ye, J. Q. Ning, Y. J. Zhong and Y. Hu, Hierarchical Cu_2S@NiCo-LDH double-shelled nanotube arrays with enhanced electrochemical performance for hybrid supercapacitors, *J. Mater. Chem. A*, 2020, **8**, 22163–22174.

25 M.-Q. Zhao, M. Torelli, C. E. Ren, M. Ghidiu, Z. Ling, B. Anasori, M. W. Barsoum and Y. Gogotsi, 2D titanium carbide and transition metal oxides hybrid electrodes for Li-ion storage, *Nano Energy*, 2016, **30**, 603–613.

26 J. H. Shi, N. X. Du, W. J. Zheng, X. C. Li, Y. Dai and G. H. He, Ultrathin Ni-Co double hydroxide nanosheets with conformal graphene coating for highly active oxygen evolution reaction and lithium ion battery anode materials, *Chem. Eng. J.*, 2017, **327**, 9–17.

27 Y. Q. Guo, X. F. Hong, Y. Wang, Q. Li, J. S. Meng, R. T. Dai, X. Liu, L. He and L. Q. Mai, Multicomponent hierarchical Cu-Doped NiCo-LDH/CuO double arrays for ultralong-Life hybrid fiber supercapacitor, *Adv. Funct. Mater.*, 2019, **29**, 1809004.

28 R. Zhang, Z. Xue, J. Q. Qin, M. Sawangphruk, X. Y. Zhang and R. P. Liu, NiCo-LDH/Ti_3C_2 MXene hybrid materials for lithium ion battery with high-rate capability and long cycle life, *J. Energy Chem.*, 2020, **50**, 143–153.

29 M. Boota, B. Anasori, C. Voigt, M.-Q. Zhao, M. W. Barsoum and Y. Gogotsi, Pseudocapacitive Electrodes produced by oxidant-

Free polymerization of pyrrole between the layers of 2D titanium carbide (MXene), *Adv. Mater.*, 2016, **28**, 1517–1522.

30 R. Z. Zhao, M. Q. Wang, D. Y. Zhao, H. Li, C. X. Wang and L. W. Yin, Molecular-level heterostructures assembled from titanium carbide mxene and Ni–Co–Al layered double-hydroxide id-state flexible asymmetric high-energy supercapacitors, *ACS Energy Lett.*, 2018, **3**, 132–140.

31 X. F. Wang, S. Kajiyama, H. Linuma, E. Hosono, S. Oro, I. Moriguchi, M. Okubo and A. Yamada, Pseudocapacitance of MXene nanosheets for high-power sodium-ion hybrid capacitors, *Nat. Commun.*, 2015, **6**, 6544.

32 Z. Ling, C. E. Ren, M.-Q. Zhao, J. Yang, J. M. Giammarco, J. S. Qiu, M. W. Barsoum and Y. Gogotsi, Flexible and conductive MXene films and nanocomposites with high capacitance, *Proc. Natl. Acad. Sci. U. S. A.*, 2014, **111**, 16676–16681.

33 Q. Zhu, H.-F. Xu, K. Shen, Y.-Z. Zhang, B. Li and S.-B. Yang, Efficient polysulfides conversion on Mo_2CT_x MXene for high-performance lithium-sulfur batteries, *Rare Met.*, 2022, **41**, 311–318.

34 J. Li, X. T. Yuan, C. Lin, Y. Q. Yang, L. Xu, X. Du, J. L. Xie, J. H. Lin and J. L. Sun, Achieving high pseudocapacitance of 2D titanium carbide (MXene) by cation intercalation and surface modification, *Adv. Energy Mater.*, 2017, **7**, 1602725.

35 M. Naguib, M. Kurtoglu, V. Presser, J. Lu, J. J. Niu, M. Heon, L. Hultman, Y. Gogotsi and M. W. Barsoum, Two-dimensional nanocrystals produced by exfoliation of Ti_3AlC_2, *Adv. Mater.*, 2011, **23**, 4248–4253.

36 Z.-M. Qiu, Y. Bai, Y.-D. Gao, C.-L. Liu, Y. Ru, Y.-C. Pi, Y.-Z. Zhang, Y.-S. Luo and H. Pang, MXenes nanocomposites for energy storage and conversion, *Rare Met.*, 2022, **41**, 1101–1128.

37 V. Kedambaimoole, K. Harsh, K. Rajanna, P. Sen, M. M. Nayakb and S. Kumar, MXene wearables: properties, fabrication strategies, sensing mechanism and applications, *Mater. Adv.*, 2022, **3**, 3784–3808.

38 N. R. Hemanth and B. Kandasubramanian, Recent advances in 2D MXenes for enhanced cation intercalation in energy harvesting applications: a review, *Chem. Eng. J.*, 2020, **392**, 123678.

39 C. D. Wang, H. Xie, S. M. Chen, B. H. Ge, D. B. Liu, C. Q. Wu, W. J. Xu, W. S. Chu, G. Babu, P. M. Ajayan and L. Song, Atomic cobalt covalently engineered interlayers for superior lithium-ion storage, *Adv. Mater.*, 2018, **30**, 1802525.

40 K. Maleski, V. N. Mochalin and Y. Gogotsi, Dispersions of two-dimensional titanium carbide MXene in organic solvents, *Chem. Mater.*, 2017, **29**, 1632–1640.

41 M. Ghidiu, S. Kota, J. Halim, A. W. Sherwood, N. Nedfors, J. Rosen, V. N. Mochalin and M. W. Barsoum, Alkylammonium cation intercalation into Ti_3C_2 (MXene): effects on properties and ion-exchange capacity estimation, *Chem. Mater.*, 2017, **29**, 1099–1106.

42 V. Shukla, The tunable electric and magnetic properties of 2D MXenes and their potential applications, *Mater. Adv.*, 2020, **1**, 3104–3121.

43 H. H. Li, Y. Ma, H. Zhang, T. Diemant, R. J. Behm, A. Varzi and S. Passerini, Metal-organic framework derived Fe_7S_8 nanoparticles embedded in heteroatom-doped carbon with lithium and sodium storage capability, *Small, Methods*, 2020, **4**, 2000637.

44 M. Sahoo and S. Ramaprabhu, One-pot environment-friendly synthesis of boron doped graphene–SnO_2 for anodic performance in Li ion battery, *Carbon*, 2018, **127**, 627–635.

45 D. Pham-Cong, S. J. Kim, S. Y. Jeong, J.-P. Kim, H. G. Kim, P. L. V. Braun and C.-R. Cho, Enhanced cycle stability of iron(II, III) oxide nanoparticles encapsulated with nitrogen-doped carbon and graphene frameworks for lithium battery anodes, *Carbon*, 2018, **129**, 621–630.

46 X. Y. Zhao, Z. Zhao-Karge, M. Fichtner and X. D. Shen, Halide-based materials and chemistry for rechargeable batteries, *Angew. Chem., Int. Ed.*, 2020, **59**, 5902–5949.

47 Z. Z. Du, W. Ai, J. Yang, Y. J. Gong, C. Y. Yu, J. F. Zhao, X. C. Dong, G. Z. Sun and W. Huang, *In situ* fabrication of Ni_2P nanoparticles embedded in nitrogen and phosphorus codoped carbon nanofibers as a superior anode for Li-Ion batteries, *ACS Sustainable Chem. Eng.*, 2018, **6**, 14795–14801.

48 S. L. Zhang, X.-Y. Li, W. T. Yang, H. J. Tian, Z. K. Han, H. J. Ying, G. X. Wang and W.-Q. Han, Novel synthesis of red phosphorus nanodot/$Ti_3C_2T_x$ MXenes from low-cost Ti_3SiC_2 MAX phases for superior lithium- and sodium-ion batteries, *ACS Appl. Mater. Interfaces*, 2019, **11**, 42086–42093.

49 Y. Y. Wen, R. Li, J. H. Liu, Z. T. Wei, S. H. Li, L. L. Du, K. Zu, Z. X. Li, Y. Y. Pan and H. Hu, A temperature-dependent phosphorus doping on $Ti_3C_2T_x$ MXene for enhanced supercapacitance, *J. Colloid Interface Sci.*, 2021, **604**, 239–247.

50 H. W. Wang, C. Wang, B. K. Dang, Y. Xiong, C. D. Jin, Q. F. Sun and M. Xu, Nitrogen, sulfur, phosphorous co-doped interconnected porous carbon nanosheets with high defect density for enhancing supercapacitor and lithium-ion battery properties, *ChemElectroChem*, 2018, **5**, 2367–2375.

51 H. S. Zhao, Y. L. Qi, K. Liang, W. K. Zhu, H. B. Wu, J. B. Li and Y. R. Ren, Phosphorus-doping and oxygen vacancy endowing anatase TiO_2 with excellent sodium storage performance, *Rare Met.*, 2022, **41**, 1284–1293.

52 S.-Y. Pang, W.-F. Io, L.-W. Wong, J. Zhao and J. H. Hao, Efficient energy conversion and storage based on robust fluoride-free self-assembled 1D niobium carbide in 3D nanowire network, *Adv. Sci.*, 2020, **7**, 1903680.

53 H. Lin, L. S. Chen, X. Y. Lu, H. L. Yao, Y. Chen and J. L. Shi, Two-dimensional titanium carbide MXenes as efficient non-noble metal electrocatalysts for oxygen reduction reaction, *Sci. China Mater.*, 2018, **62**, 662–670.

54 D. Y. Zhao, R. Z. Zhao, S. H. Dong, X. G. Miao, Z. W. Zhang, C. X. Wang and L. W. Yin, Alkali-induced 3D crinkled porous Ti_3C_2 MXene architectures coupled with NiCoP bimetallic phosphide nanoparticles as anodes for high-performance sodium-ion batteries, *Energy Environ. Sci.*, 2019, **12**, 2422–2432.

55 F. Song, R. Zhang, X. Y. Zhang, J. Q. Qin and R. P. Liu, Ni–Co double hydroxide grown on graphene oxide for enhancing lithium ion storage, *Energy Fuels*, 2020, **34**, 13032–13037.

56 X. Wang, S. Lin, H. Y. Tong, Y. N. Huang, P. Tong, B. C. Zhao, J. M. Dai, C. H. Liang, H. Wang, X. B. Zhu, Y. P. Sun and S. X. Dou, Two-dimensional V_4C_3 MXene as high performance electrode materials for supercapacitors, *Electrochim. Acta*, 2019, **307**, 414–421.

57 A. VahidMohammadi, A. Hadjikhani and S. Shahbazmohamadi, Two-dimensional vanadium carbide (MXene) as a high-capacity

cathode material for rechargeable aluminum batteries, *ACS Nano*, 2017, **11**, 11135–11144.

58 J. F. Zhou, S. Lin, Y. N. Huang, P. Tong, B. C. Zhao, X. B. Zhu and Y. P. Sun, Synthesis and lithium ion storage performance of two-dimensional V_4C_3 MXene, *Chem. Eng. J.*, 2019, **373**, 203–212.

59 Y. J. Lu, Y. J. Du and H. B. Li, Template-sacrificing synthesis of Ni-Co layered double hydroxides polyhedron as advanced anode for lithium ions battery, *Front. Chem.*, 2020, **8**, 581653.

60 S. Zhang, L. Zhang, G. C. Xu, X. L. Zhang and A. H. Zhao, The PVP-assisted construction of a $Co_3V_2O_8$@NiCo LDH hierarchical structure for high-performance lithium-ion batteries, *New J. Chem.*, 2020, **44**, 10918–10923.

61 M. Z. Yu, Z. Y. Wang, J. S. Liu, F. Sun., P. J. Yang and J. H. Qiu, A hierarchically porous and hydrophilic 3D nickel–iron/MXene electrode for accelerating oxygen and hydrogen evolution at high current densities, *Nano Energy*, 2019, **63**, 103880.

62 F. W. Ming, H. F. Liang, W. L. Zhang, J. Ming, Y. J. Lei, A.-H. Emwas and H. N. Alshareef, Porous MXenes enable high performance potassium ion capacitors, *Nano Energy*, 2019, **62**, 853–860.

63 Z. Yang, Q. H. Cheng, W. W. Li, Y. J. Li, C. Yang, K. Tao and L. Han, Construction of 2D ZIF-derived hierarchical and hollow NiCo-LDH "nanosheet-on-nanosheet" arrays on reduced graphene oxide/Ni foam for boosted electrochemical energy storage, *J. Alloys Compd.*, 2021, **850**, 156864.

64 Z. G. Wang, K. Yu, Y. Feng, R. J. Qi, J. Ren and Z. Q. Zhu, $VO_2(p)$-V_2C(MXene) grid structure as a lithium polysulfide catalytic host for high-performance Li-S battery, *ACS Appl. Mater. Interfaces*, 2019, **11**, 44282–44292.

65 M. H. Li, L. Fang, H. Zhou, F. Wu, Y. Lu, H. J. Luo, Y. X. Zhang and B. S. Hue, Three-dimensional porous MXene/NiCo-LDH composite for high performance non-enzymatic glucose sensor, *Appl. Surf. Sci.*, 2019, **495**, 143554.

66 Y. Wang, W. Zheng, P. G. Zhang, W. B. Tian, J. Chen and Z. M. Sun, Preparation of $(V_x, Ti_{1−x})_2C$ MXenes and their performance as anode materials for LIBs, *J. Mater. Sci.*, 2019, **54**, 11991–11999.

67 D. R. Liu, L. B. Wang, Y. He, L. Liu, Z. P. Yang, B. Wang, Q. X. Xia, Q. K. Hu and A. G. Zhou, Enhanced reversible capacity and cyclic performance of lithium-ion batteries using SnO_2 interpenetrated MXene V_2C architecture as anode materials, *Energy Technol.*, 2020, **9**, 2000753.

68 T. Wu and K. Liang, Caterpillar structured $Ni(OH)_2$@MnO_2 core/shell nanocomposite arrays on nickel foam as high performance anode materials for lithium ion batteries, *RSC Adv.*, 2016, **6**, 15541–15548.

69 F. F. Liu, J. Zhou, S. W. Wang, B. X. Wang, C. Shen, L. B. Wang, Q. K. Hu, Q. Huang and A. G. Zhou, Preparation of high-purity V_2C MXene and electrochemical properties as Li-Ion batteries, *J. Electrochem. Soc.*, 2017, **164**, A709.

70 R. J. Liu, L. X. Yang, G. Q. Lin, H. P. Bu, W. J. Wang, H. J. Liu and C. L. Zeng, Superior electrochemcial performances of core–shell structured vanadium oxide@vanadium carbide composites for Li-ion storage, *Appl. Surf. Sci.*, 2022, **588**, 152904.

71 P. J. Zhang, C. D. Wang, H. Q. Wei, H. W. Shou, K. F. Zhu, Y. Y. Cao, W. J. Xu, X. Guo, X. J. Wu, S. M. Chen and L. Song, 3D V_2CT_x−rGO architectures with optimized ion transport channels toward fast lithium-ion storage, *ACS Appl. Mater. Interfaces*, 2021, **13**, 61258–61266.

72 R. J. Liu, L. X. Yang, G. Q. Lin, T. Y. Zhang, H. P. Bu, H. J. Liu and C. L. Zeng, Facile fabrication of 3D flower-like $V_2Al_{1−x}CT_z$ as an anode for lithium-ion batteries, *J. Alloys Compd.*, 2022, **908**, 164596.

73 Z. J. Xie, L. M. Zhang, L. Li, Q. B. Deng, G. X. Jiang and J. Q. Wang, A ternary FeS_2/Fe_7S_8@nitrogen-sulfur co-doping reduced graphene oxide hybrid towards superior-performance lithium storage, *Prog. Nat. Sci.: Mater. Int.*, 2021, **31**, 207–214.

74 X. L. Wang, J. M. Zhang, X. Kong, X. Huang and B. Shi, Increasing rigidness of carbon coating for improvement of electrochemical performances of Co_3O_4 in Li-ion batteries, *Carbon*, 2016, **104**, 1.

75 L. W. Liang, X. Sun, C. Wu, L. R. Hou, J. F. Sun, X. G. Zhang and C. Z. Yuan, Nasicon-type surface functional modification in core–shell $LiNi_{0.5}Mn_{0.3}Co_{0.2}O_2$@$NaTi_2(PO_4)_3$ cathode enhances its high-voltage cycling stability and rate capacity toward Li-Ion batteries, *ACS Appl. Mater. Interfaces*, 2018, **10**, 5498–5510.

76 H. T. Sun, G. Q. Xin, T. Hu, M. P. Yu, D. L. Shao, X. Sun and J. Lian, High-rate lithiation-induced reactivation of mesoporous hollow spheres for long-lived lithium-ion batteries, *Nat. Commun.*, 2014, **5**, 4526.

77 K. Fang, F. Li, G.-G. Wang, Y.-L. Liu, M.-L. Tan, D.-Q. Zhao, H.-Y. Zhang and J.-C. Han, High mass-loading and binder-free flexible vanadium-based oxide cathode for zinc-ion battery *via* a bridge of MXene, *J. Mater. Sci. Technol.*, 2023, **143**, 84–92.

78 F. Dai, R. Yi, H. Yang, Y. M. Zhao, L. L. Luo, M. L. Gordin, H. Sohn, S. R. Chen, C. M. Wang, S. L. Zhang and D. H. Wang, Minimized Volume Expansion in Hierarchical Porous Silicon upon Lithiation, *ACS Appl. Mater. Interfaces*, 2019, **11**, 13257–13263.

79 F. F. Liu, S. Jin, Q. X. Xia, A. G. Zhou and L.-Z. Fan, Research progress on construction and energy storage performance of MXene heterostructures, *J. Energy Chem.*, 2021, **62**, 220–242.

80 N. Sun, Q. Z. Zhu, B. Anasori, P. Zhang, H. Liu, Y. Gogotsi and B. Xu, MXene-Bonded Flexible Hard Carbon Film as Anode for Stable Na/K-Ion Storage, *Adv. Funct. Mater.*, 2019, **29**, 1906282.

81 J. M. Wang, M. Yang, G. D. Zou, D. Liu and Q. M. Peng, Lithiation MXene Derivative Skeletons for Wide-Temperature Lithium Metal Anodes, *Adv. Funct. Mater.*, 2021, **31**, 2101180.

82 S. Barcikowski and G. Compagnini, Advanced nanoparticle generation and excitation by lasers in liquids, *Phys. Chem. Chem. Phys.*, 2013, **15**, 3022.

83 H. B. Zeng, S. K. Yang and W. P. Cai, Reshaping formation and luminescence evolution of ZnO quantum dots by laser-induced fragmentation in liquid, *J. Phys. Chem. C*, 2011, **115**, 5038–5043.

84 J. J. Deng, X. L. Yu, X. Y. Qin, D. Zhou, L. H. Zhang, H. Duan, F. Y. Kang, B. H. Li and G. X. Wang, Co–B nanoflakes as multifunctional bridges in $ZnCo_2O_4$ micro-/nanospheres for superior lithium storage with boosted kinetics and stability, *Adv. Energy Mater.*, 2019, **9**, 1803612.